Monthly Notices
of the
ROYAL ASTRONOMICAL SOCIETY

MNRAS **450,** 1085–1093 (2015) doi:10.1093/mnras/stv572

# Strong candidate for AGN feedback: VLT/X-shooter observations of BALQSO SDSS J0831+0354

Carter Chamberlain,[1]★ Nahum Arav[1]★ and Chris Benn[2]

[1]*Department of Physics, Virginia Tech, Blacksburg, VA 24061, USA*
[2]*Isaac Newton Group, Apartado 321, E-38700 Santa Cruz de La Palma, Spain*

Accepted 2015 March 12. Received 2015 February 27; in original form 2015 January 12

## ABSTRACT

We measure the location and energetics of a S IV BALQSO outflow. This outflow has a velocity of 10 800 km s$^{-1}$ and a kinetic luminosity of $10^{45.7}$ erg s$^{-1}$, which is 5.2 per cent of the Eddington luminosity of the quasar. From collisional excitation models of the observed S IV/S IV* absorption troughs, we measure a hydrogen number density of $n_{\rm H} = 10^{4.3}$ cm$^{-3}$, which allows us to determine that the outflow is located 110 pc from the quasar. Since S IV is formed in the same ionization phase as C IV, our results can be generalized to the ubiquitous C IV broad absorption lines (BALs). Our accumulated distance measurements suggest that observed BAL outflows are located much farther away from the central source than is generally assumed (0.01–0.1 pc).

**Key words:** line: formation – quasars: absorption lines – quasars: individual: SDSS J083126.15+035408.0.

## 1 INTRODUCTION

Broad absorption line (BAL) outflows are detected as absorption troughs that are blueshifted in the rest-frame spectrum of 20–40 per cent of quasars (Hewett & Foltz 2003; Dai, Shankar & Sivakoff 2008; Ganguly & Brotherton 2008; Knigge et al. 2008). From their detection rate, we deduce that these outflows cover on average ∼20–40 per cent of the solid angle around the quasar. Such large opening angles allow for efficient interaction with the surrounding medium. As shown by simulations, the mass, momentum and especially the energy carried by these outflows can play an important role in the evolution of galaxies and their environments (e.g. Scannapieco & Oh 2004; Levine & Gnedin 2005; Hopkins et al. 2006; Cattaneo et al. 2009; Ciotti, Ostriker & Proga 2009, 2010; Ostriker et al. 2010; Gilkis & Soker 2012; Choi et al. 2014). Theoretical studies show that such interactions can provide an explanation for a variety of observations: the self-regulation of the growth of the supermassive black hole (SMBH) and of the galactic bulge, curtailing the size of massive galaxies, and the chemical enrichment of the intergalactic medium. These processes are part of the so-called AGN feedback (e.g. Silk & Rees 1998; Di Matteo, Springel & Hernquist 2005; Elvis 2006; Germain, Barai & Martel 2009; Hopkins, Murray & Thompson 2009; Zubovas & Nayakshin 2014, and references therein).

The importance of quasar outflows to AGN feedback depends on the mass-flow rate ($\dot{M}$) and kinetic luminosity ($\dot{E}_{\rm k}$) of the outflowing material. An $\dot{E}_{\rm k}$ value of at least 0.5 per cent (Hopkins & Elvis 2010) or 5 per cent (Scannapieco & Oh 2004) of the Eddington luminosity ($L_{\rm Edd}$) is deemed sufficient to produce the aforementioned feedback effects. A crucial parameter needed to determine $\dot{E}_{\rm k}$ is the distance $R$ to the outflow from the central source. Lacking spatial image information, we deduce $R$ from the value of the ionization parameter ($U_{\rm H}$, see Section 4) once the hydrogen number density ($n_{\rm H}$) of the gas is known. Our group has determined $n_{\rm H}$ (leading to $R$, $\dot{M}$, and $\dot{E}_{\rm k}$) for several quasar outflows (e.g. Moe et al. 2009; Bautista et al. 2010; Dunn et al. 2010; Aoki et al. 2011; Borguet et al. 2012a) by utilizing absorption lines from excited states of singly-ionized species (e.g. Fe II* and Si II*).

Absorption troughs from singly-ionized species classify an outflow as a LoBAL. The lower detection rate of LoBALQSO in spectroscopic surveys (3–7 per cent) compared with 20–40 per cent for C IV BALQSO (Dai, Shankar & Sivakoff 2012) raises the question of whether the determinations obtained for these objects are representative of the ubiquitous high-ionization C IV BALQSO (see Dunn

**Table 1.** Physical properties of energetic quasar outflows (for full object names, see Table 5).

| Object | $v$ (km s$^{-1}$) | $R$ (pc) | $\dot{M}$ ($M_\odot$ yr$^{-1}$) | log $\dot{E}_{\rm k}$ (ergs$^{-1}$) | $\dot{E}_{\rm k}/L^{d}_{\rm Edd}$ (per cent) |
|---|---|---|---|---|---|
| J0831+0354[1] | −10 800 | 110[a] | 135 | 45.7 | 5.2 |
| J1106+1939[2] | −8250 | 320[a] | 390 | 46.0 | 12 |
| HE 0238−1904[3] | −5000 | 3400[b] | 140 | 45.0 | 0.7 |
| J0838+2955[4] | −5000 | 3300[c] | 300 | 45.4 | 2.3 |
| J0318−0600[5] | −4200 | 6000[c] | 120 | 44.8 | 0.13 |

*Notes.* $R$ from: [a]high-ionization S IV*/S IV; [b]high-ionization O IV*/O IV; [c]low-ionization Si II*/Si II; [d]See Section 5.1 for $L_{\rm Edd}$ determination.
References. (1) This work, (2) Borguet et al. (2013), (3) Arav et al. (2013), (4) Moe et al. (2009), (5) Dunn et al. (2010).

★ E-mail: carterch@vt.edu (CC); arav@vt.edu (NA)

et al. 2010). The most straightforward way to avoid such uncertainty is to observe outflows that show absorption lines from excited states of ions with a similar ionization potential to that of C IV. The optimal ion for ground-based observations is S IV (see discussion in Dunn et al. 2012; Arav et al. 2013).

To realize this, we conducted a survey using VLT/X-shooter between 2012 and 2014 aimed at finding quasar outflows showing absorption from S IV λ1062.66 and the excited state S IV* λ1072.97. Of the 24 objects observed, two objects (SDSS J1106+1939 and SDSS J1512+1119) have been published (Borguet et al. 2013, hereafter Paper I). SDSS J1106+1939 yielded the most energetic S IV BAL outflow to date with $\dot{E}_{\rm k} = 10^{46.0}$ erg s$^{-1}$ (see Section 5.3 for further discussion), whereas the SDSS J1512+1119 outflow has $\dot{E}_{\rm k} \lesssim 10^{43.8}$ erg s$^{-1}$. In this paper, we present the analysis of an outflow from SDSS J0831+0354, which exhibits similar properties to that of SDSS J1106+1939. This includes the presence of P V and S IV/S IV* troughs, thereby allowing us to determine the distance and energetics (see Section 5.1) of the SDSS J0831+0354 outflow. Table 1 summarizes the current state of the field by listing the energetics of prominent outflows analysed by our group.

The plan of this paper is as follows. In Section 2, we present the VLT/X-shooter observations of SDSS J0831+0354. In Section 3, we identify the absorption troughs of the outflow and measure the ionic column densities which are used to determine the number density (Section 3.4) and the photoionization solution (Section 4). In Section 5, we determine the outflow distance and energetics and compare them to outflows from other objects. We summarize our method and findings in Section 6.

## 2 OBSERVATIONS AND DATA REDUCTION

SDSS J0831+0354 (J2000: RA = 08 31 26.15, DEC = +03 54 08.0, $z = 2.0761$) was observed with VLT/X-shooter ($R \sim 6000$–$9000$, see Paper I for instrument specifications) as part of our programme 92.B-0267 (PI: Benn) in 2014 January with a total integration time of 10 640 s.

We reduced the SDSS J0831+0354 spectra in a similar fashion to those of SDSS J1106+1939 (detailed in Paper I): we rectified and wavelength calibrated the two-dimensional spectra using the ESO Reflex workflow (Ballester et al. 2011), then extracted one-dimensional spectra using an optimal extraction algorithm and finally flux calibrated the resulting data with the spectroscopic observations of a standard star observed the same day as the quasar. The one-dimensional spectra were then co-added after manually performing cosmic ray rejection on each spectra. We present the reduced UVB+VIS spectrum of SDSS J0831+0354 in Fig. 1.

## 3 SPECTRAL FITTING

Absorption troughs associated with H I, C IV, N V, Mg II, Al III, Si III, Si IV, P V, and S IV/S IV* ionic species are seen in the spectrum (see Fig. 1). The high velocity ($v = -10\,800$ km s$^{-1}$) and width (3500 km s$^{-1}$) of the C IV trough satisfies the definition of a BAL outflow (i.e. $v_{\rm max} > 5000$ km s$^{-1}$ and width >2000 km s$^{-1}$, see Weymann, Carswell & Smith 1981). The balnicity index of the C IV trough is 1100 km s$^{-1}$ (see Weymann et al. 1991).

### 3.1 Unabsorbed emission model

We correct the spectrum for galactic extinction ($E(B-V) = 0.025$; Schlegel, Finkbeiner & Davis 1998) using the reddening curve of Cardelli, Clayton & Mathis (1989). We then fit the continuum with a cubic spline resembling a power law of the form $F(\lambda) = F_{1100}(\lambda/1100)^{\alpha}$, where $F_{1100} = 1.58 \times 10^{-16}$ erg s$^{-1}$ cm$^{-2}$ Å$^{-1}$ is the observed flux at 1100 Å (rest frame) and $\alpha \simeq -1.16$. We model the broad emission lines (BELs) with a sum of one to three Gaussians, which do not significantly affect the column density extraction for most ions since the high velocity of the outflow ($v = -10\,800$ km s$^{-1}$) shifts the BALs far from the wings of their corresponding BELs. However, the S IV and S IV* BALs lie within the O VI BEL, which we model by scaling the C IV BEL template to match the peak emission of the S IV BAL region.

### 3.2 The blended troughs

We model the optical depth of the absorption troughs with three Gaussians

$$\tau(v) = \sum_{i=1}^{3} \tau_i \exp\left[\frac{-(v-v_i)^2}{2\sigma_i^2}\right] \qquad \mathrm{FWHM} = 2\sqrt{2\ln 2}\,\sigma \qquad (1)$$

with the same centroid and width in all the observed ionic troughs. Our first Gaussian ($v_1 = -12\,100$ km s$^{-1}$, FWHM = 1460 km s$^{-1}$) is chosen specifically to match the blue wing of the Si IV λ1393.75 line, as well as the blue wing of the Al III λ1854.72 line. The second Gaussian ($v_2 = -10\,800$ km s$^{-1}$, FWHM = 940 km s$^{-1}$), which represents the majority of the absorption, targets the Si IV and P V doublets. A third Gaussian ($v_3 = -10\,000$ km s$^{-1}$, FWHM = 590 km s$^{-1}$) is needed to match the red wing of the Al III λ1862 line, as well as the red wing of the C IV and N V blends. These three Gaussians form the template used to extract the column density (following the same procedure as Paper I) from the observed troughs of all ions except for P V and Si III, which will be discussed in the next section. For the three Gaussian template, we use a covering factor ($C_{\rm ion}$) that is constant throughout the trough (i.e. for all three Gaussians), and varies only between ions. For a description of the partial covering (PC) model, see Arav et al. (2008). For ions detected by a singlet, we take the apparent optical depth (AOD) measurement as a lower limit.

### 3.3 Velocity-dependent covering: P V and Si III

Although the central Gaussian of our template (see Section 3.2) can be used to model the P V and Si IV doublet troughs, the ratio between the red and the blue components of each doublet approaches 1:1. This suggests that the troughs are strongly influenced by the velocity-dependent PC of the emission source (see Arav et al. 1999b; Borguet et al. 2012b). Due to the presence of Ly$\alpha$ forest-intervening troughs, we proceed by modelling the normalized flux of the doublets with a smooth function. For phenomenological flexibility, we built a function from the product of two logistic functions (hereafter logistic fit)

$$I(v) = 1 - \frac{A}{\left(1+e^{w_{\rm b}(v-v_{\rm b})}\right)\left(1+e^{w_{\rm r}(v-v_{\rm r})}\right)}, \qquad (2)$$

where $A$ is the maximum depth of the logistic fit, $v_{\rm b}$ and $v_{\rm r}$ are the velocities of the blue and red wing half-maximums, respectively ($v_{\rm b} \leq v_{\rm r}$), and $w_{\rm b}$ and $w_{\rm r}$ are the slope/variance of the blue and red wings, respectively ($w_{\rm b} < 0 < w_{\rm r}$). This function is particularly suited to fitting asymmetric troughs.

We model each P V doublet component (normalized and in velocity-space) using a logistic fit, and determine the velocity-dependent covering fraction and optical depth solution (using equation 3 of Dunn et al. 2010). Integrating this optical depth over the trough yields the P V column density for the PC model given in Table 2.

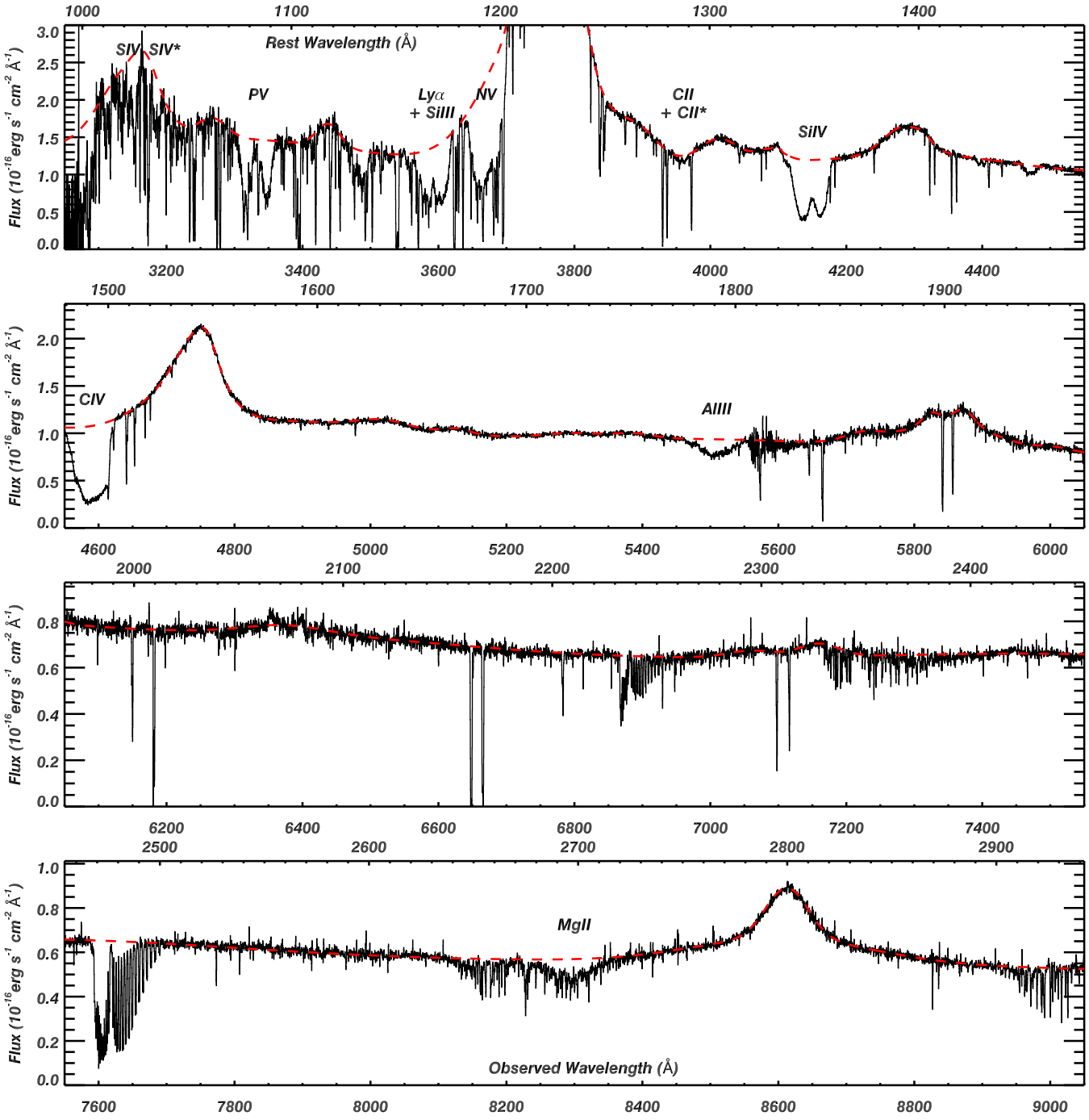


**Figure 1.** VLT/X-shooter spectrum of the quasar SDSS J0831+0354 ($z = 2.0761$). We label the ionic absorption troughs associated with the outflow, and represent the unabsorbed emission model with the red dashed line (see Section 3.1). Narrow absorption from intervening systems appear throughout the spectrum, and terrestrial absorption from molecular $O_2$ in our atmosphere is seen near 6850 and 7600 Å observed frame, but none of these features affect the analysis presented here.

Si III is a singlet, thus, we cannot determine a covering model for this ion. Therefore, we use the covering factor of Si IV as a proxy to extract the Si III PC column density given in Table 2, since Si IV is the next ionization stage of the same element. The lower error of 0.11 dex for the adopted Si III measurement includes systematic errors in continuum placement and blending of the intervening Ly$\alpha$ forest. We note that, by coincidence, the difference between the PC measurement and the AOD measurement is also 0.11 dex.

### 3.4 The density-sensitive troughs: S IV and S IV*

The column densities from S IV and its excited state S IV* play an essential role in our analysis: the ratio of level populations between S IV* and S IV is dictated by collisional excitation, which depends on $n_e$ and is relatively insensitive to temperature (see fig. 8 of Paper I).

As in the case of Si III, S IV $\lambda$1062.66 and S IV* $\lambda$1072.97 are both singlets (the lines arise from different energy levels with a priori

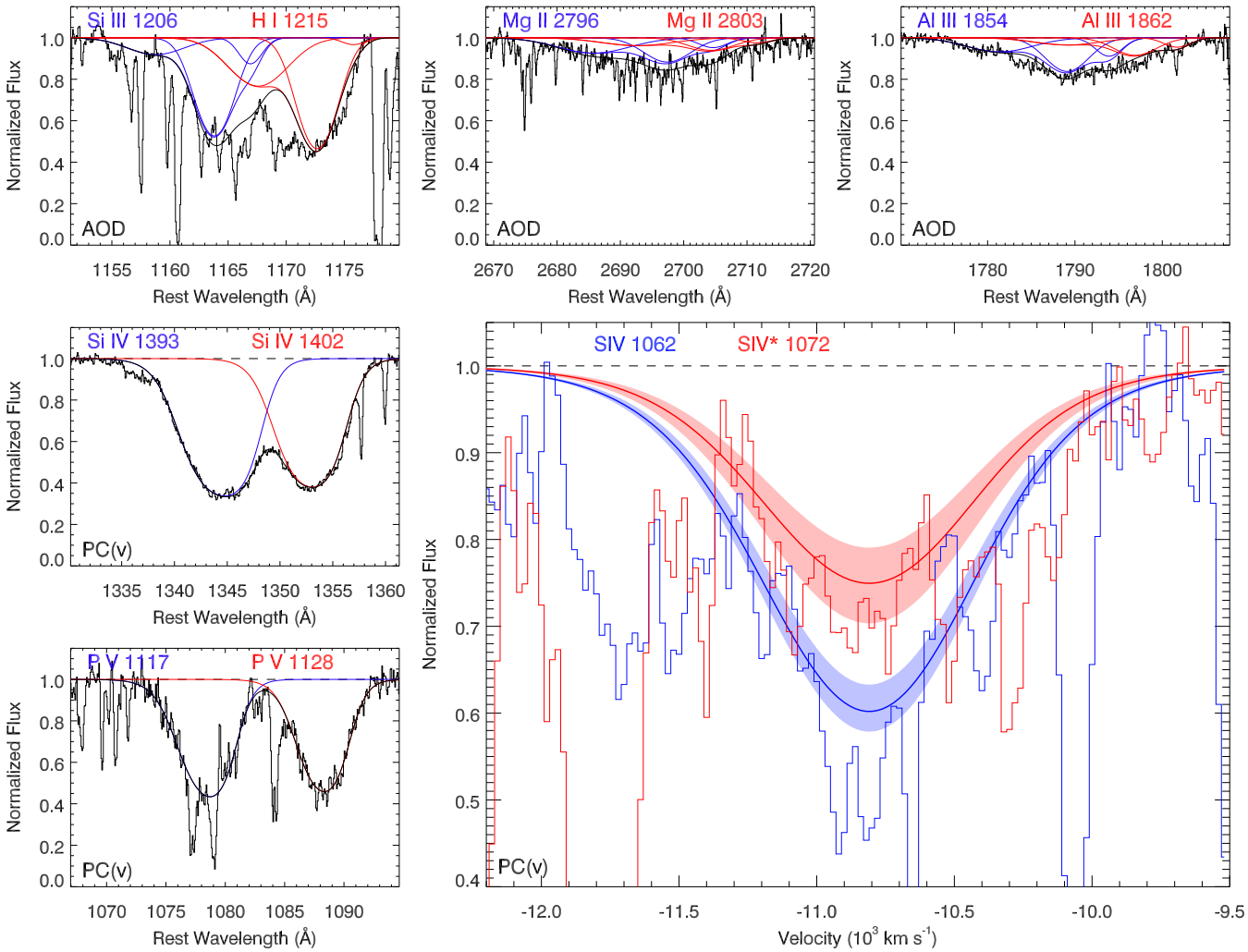


**Figure 2.** Fits to the absorption troughs observed in the X-shooter spectrum of SDSS J0831+0354. Each trough is fit by scaling the optical depths of three template Gaussians whose centroid and width are fixed among the ions (see Section 3.2). The Gaussian templates for each transition are shown in the same colour (red or blue), and the combined absorption from blended lines is represented as a black solid line. The first row of plots show the AOD fits to Si III (and H I), Mg II, and Al III. Due to the influence of non-black saturation in the Si IV and P V troughs (see in text), we show the velocity-dependent partial covering (PC(v)) fit to those ions. The plot in the lower-right shows the PC(v) fit to the S IV and S IV* troughs in velocity space. The fits are spanned by shaded contours representing the upper and lower errors assigned to the fits.

undetermined populations), thus a velocity-dependent covering solution cannot be determined from these two lines alone. Therefore, we follow the same method as with Si III, using the velocity-dependent covering template of Si IV to model the S IV/S IV* troughs with the PC(v) method.

We begin this method by modelling the S IV/S IV* troughs using a logistic curve that closely resembles the central Gaussian of the three Gaussian template. This resemblance ensures that the S IV absorption model is kinematically related to the other ionic troughs in the outflow. The logistic curve was fit to the S IV troughs by scaling the amplitude until it fit the broad absorption features in the spectrum while excluding the narrow Ly$\alpha$ troughs. To assign the upper and lower errors to this fit, we again scale the depth of the logistic template until the resulting template clearly over- or underpredicts significant portions of the broad absorption trough. The quality of this fit and of the stated errors can be judged in the lower-right panel of Fig. 2.

The optical depth of the fit (and its errors) was translated to S IV/S IV* column density measurements using the same procedure as in Si III (i.e. adopting the velocity-dependent covering solution for Si IV). These column densities are reported in the fourth column of Table 2. A similar value (differing by only 0.05 dex) was obtained with the P V velocity-dependent covering template, demonstrating the robustness of this method.

To obtain the AOD column density, we follow the same procedure as the PC(v) modelling, instead using the central Gaussian of the three Gaussian template described in Section 3.2. For completion, we also apply the *constant* PC template of Si IV to the S IV/S IV* absorption (using the central Gaussian as the optical depth template), and report the PC column density in the third column of Table 2.

We deduce the $n_e$ of the outflow by comparing the S IV*/S IV column density ratio to predictions (see Fig. 3) made with the Chianti 7.1.3 atomic data base (Landi et al. 2013). Using the column densities for S IV and S IV* reported in Table 2 and the electron temperature found for our best-fitting CLOUDY models from Section 4 (9000 K, a weighted average for S IV across the slab), we find $\log(n_e) = 4.42^{+0.26}_{-0.22}$ cm$^{-3}$ by averaging the two absorption models (reported in Table 3) and adding their errors in quadrature.

**Table 2.** SDSS J0831+0354 log column densities ($cm^{-2}$) for the three absorption models AOD, PC, and PC(v) (velocity-dependent covering). Upper limits are shown in red and lower limits are in blue.

| Ion | AOD | PC | PC(v) | Adopted[a] |
|---|---|---|---|---|
| H I | $>14.96$ | $>15.17$ | – | $>15.17$ |
| He I* | $<15.14$ | – | – | $<15.14$ |
| C II | $<14.46$ | – | – | $<14.46$ |
| C IV | $>15.50$ | $>15.65$ | – | $>15.65$ |
| N V | $>15.60$ | $>15.79$ | – | $>15.79$ |
| Mg II | $>13.78$ | $13.87^{+0.13}_{-0.13}$ | – | $13.87^{+0.13}_{-0.13}$ |
| Al II | $<13.07$ | – | – | $<13.07$ |
| Al III | $>14.10$ | $14.27^{+0.13}_{-0.13}$ | – | $14.27^{+0.13}_{-0.13}$ |
| Si III | $>14.27$ | $>14.35$ | $>14.38$ | $>14.38^{b}_{-0.11}$ |
| Si IV | $>15.17$ | $>15.44$ | $>15.40$ | $>15.40$ |
| P V | $>15.18$ | $15.33^{+0.05}_{-0.05}$ | $15.47^{+0.15}_{-0.10}$ | $15.47^{+0.15}_{-0.10}$ |
| S IV | $>15.53$ | $15.48^{+0.07}_{-0.10}$ | $15.60^{+0.04}_{-0.05}$ | $15.60^{+0.04}_{-0.05}$ |
| S IV* | $>15.35$ | $15.40^{+0.07}_{-0.12}$ | $15.39^{+0.10}_{-0.10}$ | $15.39^{+0.10}_{-0.10}$ |

*Notes.* [a]Adopted value for photoionization modelling (see in text).
[b]We use the difference between the Si III, AOD, and PC measurements as a lower error on the Si III lower limit.

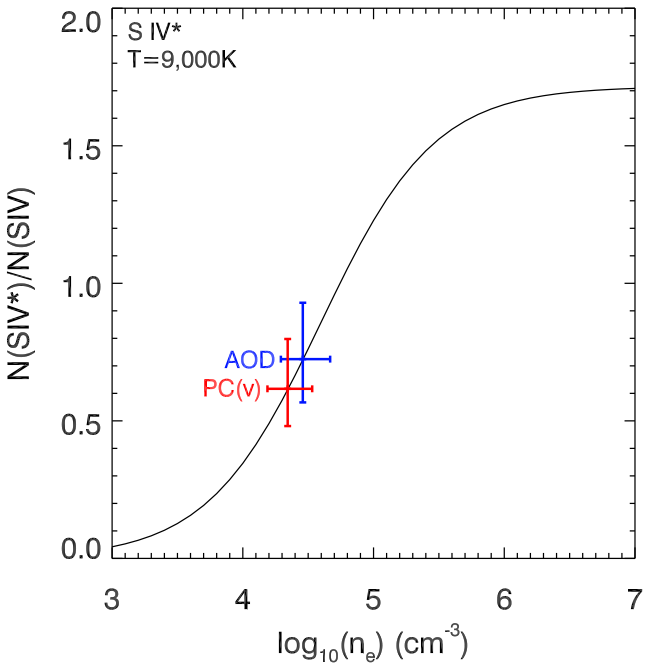


**Figure 3.** Density diagnostic using the S IV*/S IV ratio for the SDSS J0831+0354 outflow, presented in the same manner as Paper I: we plot the S IV*/S IV theoretical ratio versus electron number density and overlay our measured value (for two absorber models, AOD, and velocity-dependent PC(v)) to determine the number density and its errors.

## 4 PHOTOIONIZATION ANALYSIS

We use photoionization models in order to determine the ionization equilibrium of the outflow, its total hydrogen column density ($N_{\rm H}$), and to constrain its metallicity. The ionization parameter

$$U_{\rm H} \equiv \frac{Q_{\rm H}}{4\pi R^2 c n_{\rm H}}, \quad (3)$$

(where $Q_{\rm H}$ is the source emission rate of hydrogen ionizing photons, $R$ is the distance to the absorber from the source, $c$ is the speed of light, and $n_{\rm H}$ is the hydrogen number density) and $N_{\rm H}$ of the outflow are determined by self-consistently solving the ionization and thermal balance equations with version c08.01 of the spectral synthesis code CLOUDY, last described in Ferland et al. (2013). We assume a plane-parallel geometry for a gas of constant $n_{\rm H}$ and initially choose solar abundances and the UV-Soft spectral energy distribution (SED) which is a good representation of radio-quiet quasars (described in section 4.2 of Dunn et al. 2010, other SEDs, and metallicities will be explored in Section 4.2 here). For the chosen SED and metallicity, we generate a grid of models by varying $N_{\rm H}$ and $U_{\rm H}$. Ionic column densities ($N_{\rm ion}$) predicted by the models are tabulated and compared with the measured values in order to determine the models that best reproduce the measured $N_{\rm ion}$. For a more elaborate description of this method, see Paper I and Arav et al. (2013).

**Table 3.** Number density measurements. The values correspond to the horizontal error bars in Fig. 3.

| | AOD | PC(v) | Adopted |
|---|---|---|---|
| $\log(n_{\rm e})$ | $4.47^{+0.21}_{-0.18}$ | $4.36^{+0.19}_{-0.16}$ | $4.42^{+0.26}_{-0.22}$ |

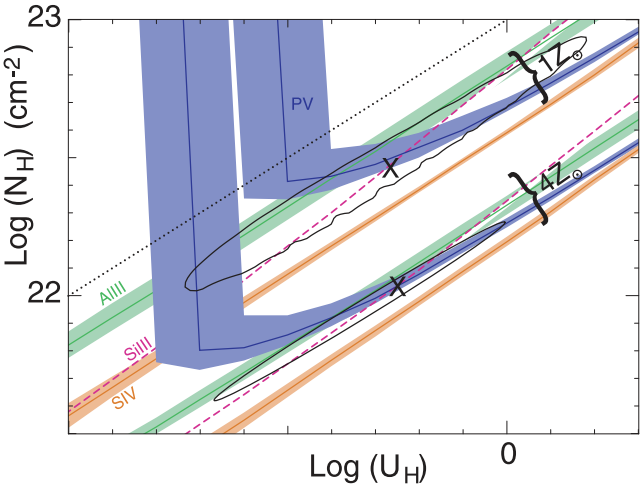


**Figure 4.** Phase plot showing the photoionization solution using the UV-Soft SED for gas with one and four times solar metallicity. Each coloured contour represents (for one of the two metallicities) the locus of models ($U_{\rm H}$, $N_{\rm H}$) which predict a column density consistent with the observed column density for that ion. The bands which span the contours are the $1\sigma$ uncertainties in the measured observations. The dashed line indicates the Si III lower limit. For each metallicity, the black 'X' is the best ionization solution and is surrounded by the $\chi^2$ contour (see in text).

### 4.1 Photoionization solution

In Fig. 4, contours where model predictions match the measured $N_{\rm ion}$ are plotted in the $N_{\rm H}$–$U_{\rm H}$ plane. Note that Fig. 4 presents models for two different metallicity values ($1Z_{\odot}$ and $4Z_{\odot}$, see discussion in Section 4.2). The ionic column densities used in the photoionization modelling are listed in the last column of Table 2, consisting of the PC measurements where available and with PC(v) prioritized over PC. In Fig. 4, we show only the ions which dominate the solution; the lower limits (H I, C IV, N V, and Si IV) and upper limits (He I*, C II, and Al II) are trivially satisfied by the constraints of Al III and

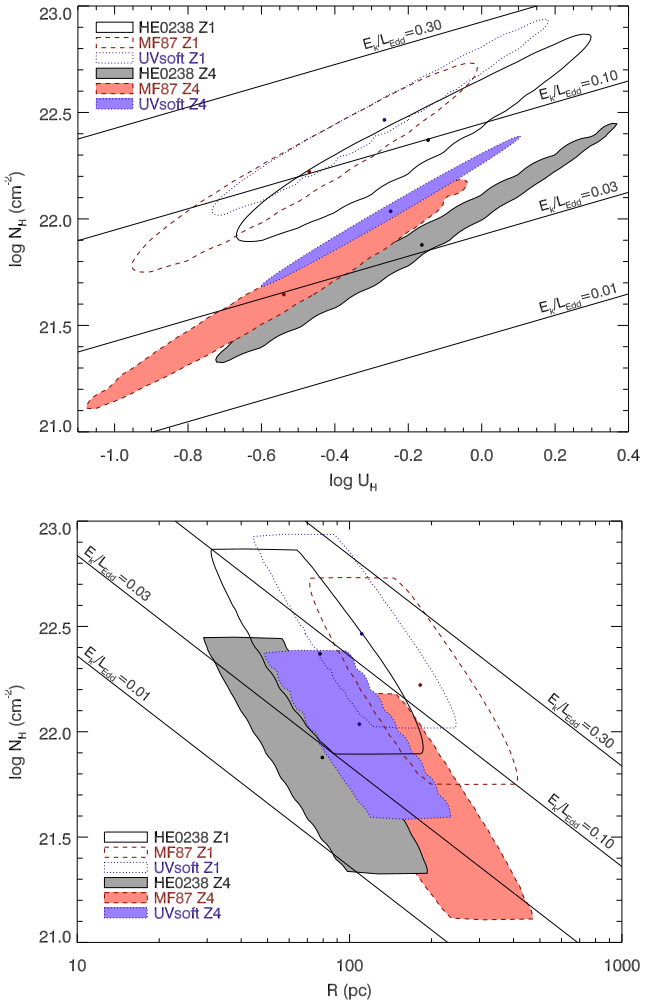


**Figure 5.** Top: phase plot showing the photoionization solution for three SEDs (HE0238, MF87, and UV-Soft, see descriptions in Arav et al. 2013) and two metallicities (one solar (Z1) and four solar (Z4)) for a total of six models. Contours of equal $\dot{E}_k/L_{Edd}$ (assuming fixed $n_H$) are shown as parallel, thin solid lines assuming the UV-Soft SED (see in text). Bottom: same as above, but with the horizontal axis converted to distance, which incorporates the errors on $n_H$ and $U_H$ into the horizontal errors on $R$.

S IV. The Mg II contour lies between the Al III and S IV contours, and is thus also satisfied.

For $Z = 1\,Z_\odot$, the P V contour requires a higher $N_H$ than the S IV contour in regions also satisfied by the Si III lower limit (above the dashed line in Fig. 4). This overprediction of the S IV column density will be discussed in Section 5.2. The solution is also influenced by the Al III contour which lies parallel to S IV. This results in a poor fit ($\chi^2_{red} = 10.6$), since no models can simultaneously predict the observed S IV and Al III column densities.

### 4.2 Dependence on SED and metallicity

We consider the sensitivity of the photoionization solution to our choice of SED and metallicity by following the approach of Arav et al. (2013), thereby allowing for comparison with previous outflows under the same set of assumptions. We find the photoionization solution in six different cases (three SEDs from Arav et al. 2013 each with $1\,Z_\odot$ and $4\,Z_\odot$), plot the $\chi^2$ contours in the top panel of Fig. 5 and report the solutions in Table 5. The change in metallicity from $1\,Z_\odot$ to $4\,Z_\odot$, scaled according to the CLOUDY starburst schema (following grid M5a of Hamann & Ferland 1993), has the same effect with each SED, decreasing the $\log(N_H)$ of the solution by 0.4 dex. This is illustrated in Fig. 4, which shows the photoionization solution for metallicities of both $Z = 1\,Z_\odot$ and $4\,Z_\odot$. We will discuss alternative elemental abundances in Section 5.2; here, we consider the same metallicities used for other outflows studied by our group.

**Table 4.** Properties of the chosen SEDs.

| SED | HE0238 | MF87 | UV-Soft |
|---|---|---|---|
| $\log(L_{Bol})$ (erg s$^{-1}$) | 46.79 | 47.03 | 46.87 |
| $\log(Q_H)$ (s$^{-1}$) | 56.53 | 56.95 | 56.72 |

The different SEDs we use spread the solution over 0.4 dex in $\log(U_H)$, which is comparable to the errors on each solution. In Table 4, we report $Q_H$ as well as the bolometric luminosity $L_{Bol}$ for the three SEDs by fitting them to the measured flux (corrected for Galactic reddening) at 1100 Å (in the rest frame) and integrating over the whole energy range.

One important motivation to find both the ionization parameter $U_H$ and the number density $n_H$ is to determine the distance of the outflow $R$ from equation (3). We therefore convert the ionization parameter $\log(U_H)$ to distance $R$ using equation (3) and present the same six photoionization solutions in the bottom panel of Fig. 5. The uncertainties on $U_H$ and $n_H$ are incorporated into our value for $R$, which forms the horizontal spread of the contours in Fig. 5. Since $N_H$ is not involved in the distance determination, the vertical spread of the contours in Fig. 5 remains unchanged. In both panels of Fig. 5, we also show the contours of equal $\dot{E}_k/L_{Edd}$ (see Section 5.1) assuming the UV-Soft SED, noting that the same contours for the different SEDs are shifted in $\log(N_H)$ by no more than 0.1 dex.

## 5 RESULTS AND DISCUSSION

### 5.1 Energetics

Assuming the outflow is in the form of a thin partial shell, its mass-flow rate ($\dot{M}$) and kinetic luminosity ($\dot{E}_k$) are given by (see Borguet et al. 2012a, for discussion)

$$\dot{M} = 4\pi R \Omega \mu m_p N_H v \quad (4)$$

$$\dot{E}_k = 2\pi R \Omega \mu m_p N_H v^3, \quad (5)$$

where $R$ is the distance from the outflow to the central source, $\Omega$ is the global covering fraction of the outflow, $\mu = 1.4$ is the mean atomic mass per proton, $m_p$ is the mass of the proton, $N_H$ is the total hydrogen column density of the absorber, and $v$ is the radial velocity of the outflow. Using the parameters reported in the preceding sections, we calculate the energetics for the six models we have considered for the S IV outflow of SDSS J0831+0354 and report the relevant values in the first six rows of Table 5 (the other four rows are comparison outflows that will be discussed in Section 5.3). We adopt the UV-Soft SED with $Z = 4\,Z_\odot$ as our representative model for this outflow, which is the same model chosen in Paper I, and yields a conservative measurement of $\dot{E}_k$. As in Paper I, we use $\Omega = 0.08$, which is appropriate for S IV BAL outflows.

As noted in the Introduction, an $\dot{E}_k$ value of at least 0.5 per cent (Hopkins & Elvis 2010) or 5 per cent (Scannapieco & Oh 2004)

**Table 5.** Physical properties of energetic quasar outflows.

| Object[a], SED | $\log(L_{\rm Bol})$ (erg s$^{-1}$) | $v$ (km s$^{-1}$) | $\log(U_{\rm H})$ | $\log(N_{\rm H})$ (cm$^{-2}$) | $\log(n_{\rm e})$ (cm$^{-3}$) | $R$ (pc) | $\dot{M}$ (M$_\odot$ yr$^{-1}$) | $\log(\dot{E}_{\rm k})$ (erg s$^{-1}$) | $\dot{E}_{\rm k}/L_{\rm Edd}$ (per cent) |
|---|---|---|---|---|---|---|---|---|---|
| SDSS J0831+0354 HE0238 Z1 | 46.8 | −10 800 | $-0.15^{+0.4}_{-0.5}$ | $22.4^{+0.5}_{-0.5}$ | $4.42^{+0.26}_{-0.22}$ | $78^{+27}_{-18}$ | $230^{+330}_{-130}$ | $45.9^{+0.4}_{-0.3}$ | $8^{+11}_{-4.4}$ |
| SDSS J0831+0354 MF87 Z1 | 47.0 | −10 800 | $-0.47^{+0.5}_{-0.5}$ | $22.2^{+0.5}_{-0.5}$ | $4.42^{+0.26}_{-0.22}$ | $180^{+53}_{-44}$ | $390^{+570}_{-220}$ | $46.1^{+0.4}_{-0.4}$ | $13^{+19}_{-7.5}$ |
| SDSS J0831+0354 UV-Soft Z1 | 46.9 | −10 800 | $-0.26^{+0.4}_{-0.5}$ | $22.5^{+0.5}_{-0.4}$ | $4.42^{+0.26}_{-0.22}$ | $110^{+30}_{-25}$ | $410^{+530}_{-220}$ | $46.2^{+0.4}_{-0.3}$ | $14^{+18}_{-7.7}$ |
| SDSS J0831+0354 HE0238 Z4 | 46.8 | −10 800 | $-0.16^{+0.5}_{-0.6}$ | $21.9^{+0.6}_{-0.6}$ | $4.42^{+0.26}_{-0.22}$ | $79^{+33}_{-24}$ | $76^{+120}_{-46}$ | $45.4^{+0.4}_{-0.4}$ | $2.6^{+4.2}_{-1.6}$ |
| SDSS J0831+0354 MF87 Z4 | 47.0 | −10 800 | $-0.54^{+0.5}_{-0.5}$ | $21.6^{+0.5}_{-0.5}$ | $4.42^{+0.26}_{-0.22}$ | $200^{+74}_{-54}$ | $110^{+170}_{-66}$ | $45.6^{+0.4}_{-0.4}$ | $3.8^{+5.8}_{-2.3}$ |
| SDSS J0831+0354 UV-Soft Z4 | 46.9 | −10 800 | $-0.25^{+0.3}_{-0.4}$ | $22.0^{+0.4}_{-0.5}$ | $4.42^{+0.26}_{-0.22}$ | $110^{+27}_{-15}$ | $150^{+140}_{-84}$ | $45.7^{+0.3}_{-0.4}$ | $5.2^{+4.8}_{-2.9}$ |
| SDSS J1106+1939 UV-Soft Z4 | 47.2 | −8250 | $-0.5^{+0.3}_{-0.2}$ | $22.1^{+0.3}_{-0.1}$ | $4.1^{+0.02}_{-0.37}$ | $320^{+200}_{-100}$ | $390^{+300}_{-10}$ | $46.0^{+0.3}_{-0.1}$ | $12^{+11}_{-0.3}$ |
| HE 0238−1904 Z4[b] | 47.2 | −5000 | $0.5^{+0.1}_{-0.1}$ | $20.0^{+0.1}_{-0.1}$ | $3.83^{+0.10}_{-0.10}$ | $3400^{+2000}_{-490}$ | $140^{+80}_{-40}$ | $45.0^{+0.2}_{-0.2}$ | $0.7^{+0.5}_{-0.2}$ |
| SDSS J0838+2955 | 47.5 | −5000 | $-2.0^{+0.2}_{-0.2}$ | $20.8^{+0.3}_{-0.3}$ | 3.8 | $3300^{+1500}_{-1000}$ | $300^{+210}_{-120}$ | $45.4^{+0.2}_{-0.2}$ | $2.3^{+1.5}_{-0.8}$ |
| SDSS J0318−0600 | 47.7 | −4200 | −3.1 | 19.9 | 3.3 | 6000 | 120 | 44.8 | 0.13 |

[a]All objects are from the SDSS survey, except for HE 0238-1904. [b]For the high-ionization phase of trough B.

of the Eddington luminosity ($L_{\rm Edd}$) is deemed sufficient to produce significant AGN feedback effects. We determine the Eddington luminosity $L_{\rm Edd} = 10^{47.0}$ erg s$^{-1}$ from the mass of the SMBH (e.g. using equation 6.21 of Krolik 1999). The mass of the SMBH is determined using the virial mass estimator from equation (3) of Park et al. (2013, given the caveat that the scaling relationship extrapolated to high-$z$/luminosity quasars is not yet firmly established). This estimate requires the continuum luminosity at rest-frame 1350 Å and the FWHM (full width at half-maximum) of the C IV BEL, both of which are directly measured from our spectrum. We use this method to determine $L_{\rm Edd}$ for the quasars SDSS J1106+1939 and SDSS J0838+2955. The C IV BEL in SDSS J0318−0600 is not well defined, so we perform a similar analysis using the Mg II BEL and equation (1) of Vestergaard & Osmer (2009). The only spectral coverage of HE 0238−1904 is in the extreme-UV, which does not cover any diagnostic lines sufficient for this method. We therefore use the assertion (from section 9 of Arav et al. 2013) that the Eddington luminosity is approximately the bolometric luminosity for our comparison in Table 1.

We note that recent studies (Luo et al. 2014) have found X-ray weak SEDs for BALQSO that are much softer than the UV-Soft SED we use here. To explore the effects of such an SED on our results, we constructed an SED from the object in Luo et al. (2014) showing the most extreme X-ray softness (PG 1254+047) by interpolating between the given flux points (see right-centre panel of fig. 3 of Luo et al. 2014). At 2 keV, the flux is three orders of magnitude lower than in our UV-Soft SED. The photoionization solution for this very soft SED leads to a distance of 51 pc and $\dot{E}_{\rm k} = 10^{44.9}$ erg s$^{-1}$ for the outflow using $Z = 4{\rm Z}_\odot$. This distance and energy is lower by a factor of 2 and 6, respectively, compared to the values obtained with the UV-Soft SED (110 pc, $\dot{E}_{\rm k} = 10^{45.7}$ erg s$^{-1}$) for $Z = 4{\rm Z}_\odot$.

We caution that the cause of the observed X-ray weakness can be attributed to optically thick absorption from the outflow itself, rather than intrinsically weak X-ray emission or obscuration between the central source and the outflow. If this is the case, then the SED incident on the outflow would likely resemble one of the other SEDs presented here. It is the incident radiation that will determine the photoionization solution.

### 5.2 The S IV discrepancy

Our photoionization solution (for the UV-Soft SED) overpredicts the S IV total column density by a factor of 8, which is not alleviated appreciably by changing the SED or metallicity. We offer two resolutions to this discrepancy: a two-phase solution, or individual abundance scaling of sulphur.

(1) Arav et al. (2013) showed that two ionization phases exist in some outflows (in that case smaller, denser cloudlets embedded in high-ionization gas with much larger $N_{\rm H}$), and can account for the appearance of low-ionization species that are inconsistent with the ionization solution obtained from higher-ionization species. S IV and P V are both high-ionization species, thus their column densities can be produced in a separate phase than the low-ionization species (Mg II and Al III). The S IV and P V contours in Fig. 4 converge at high-ionization parameters ($\log U_{\rm H} > 0.3$). A high-ionization phase at this ionization parameter would satisfy both the S IV and P V constraints, but underpredict the Mg II and Al III column densities, which would need to be satisfied by a low-ionization solution. A two-phase solution could resolve the S IV discrepancy, but such a solution is not well-constrained with the measurements obtained from our spectra. However, any high-ionization solutions that adhere to the P V constraint would move towards the upper-right corner of Fig. 4. Since $\dot{E}_{\rm k} \propto N_{\rm H}/\sqrt{U_{\rm H}}$, this increase in both $U_{\rm H}$ and $N_{\rm H}$ by 0.6 dex would result in an increase in $\dot{E}_{\rm k}$ of 0.3 dex.

(2) The discrepancy between S IV and the other ions may be alleviated by considering a higher metallicity, as outflows are known to have supersolar metallicities (e.g. Gabel, Arav & Kim 2006; Arav et al. 2007). In our CLOUDY models, the discrepancy persists with different metallicities since the abundance scaling schema from grid M5a of Hamann & Ferland (1993) does not increase the relative [S/P] or [S/Al] abundances. An alternative enrichment model that results in [S/P] = −0.9 and [S/Al] = −0.9 for a certain metallicity would decrease the S IV column density predicted by the solution from the P V and Al III constraints by a factor of 8, thus eliminating the discrepancy that appeared in the solar abundances case. Considering the absence of a complete AGN abundance scaling model, this solution is not as implausible as it seems; e.g. Ballero et al. (2008) derives relative abundances such as [Si/C] = 0.83 for $Z = 7.22\,{\rm Z}_\odot$.

If neither of these scenarios apply, then, we conclude that the S IV column density is indeed a factor of 8 higher than was measured from the S IV and S IV* troughs, and one or both of the troughs must be saturated. S IV* cannot be saturated since its trough is shallower than S IV (see discussion in section 6.3 of Paper I), thus the true S IV column density increases by a factor of 8, and the S IV*/S IV column density ratio decreases by the same factor. This correction would decrease $n_{\rm e}$ by an order of magnitude (see Fig. 3), which would increase $R$ by a factor of 3 (see equation 3), and increase $\dot{M}$ and $\dot{E}_{\rm k}$

by a factor of 3 (see equation 5). Although this effect would enhance the energetics of the outflow, we suspect that S IV is not saturated since the depth of S IV λ1062.66 is shallower than either line from the P V doublet which is presumed much closer to saturation. As S IV and P V are both high-ionization ions, we assume that they have similar covering factors and thus, their absorption lines would be the same depth if saturated.

### 5.3 Comparison with other outflows

In Table 5, we also list four other outflows with the highest $\dot{E}_k$ determined by our group. Two of these are low-ionization BALs that appear in SDSS J0838+2955 (Moe et al. 2009) and SDSS J0318−0600 (Dunn et al. 2010), and their distance estimate is based on singly-ionized species. This introduces an uncertainty (see Section 1 for discussion) that can be alleviated by utilizing metastable levels from high-ionization ions such as S IV/S IV*.

The first object to show a large kinetic luminosity ($\dot{E}_k = 10^{46}$ erg s$^{-1}$) using S IV/S IV* absorption was SDSS J1106+1939 (Paper I). The outflow we study in this paper (SDSS J0831+0354) is the second such example, and it exhibits properties similar to SDSS J1106+1939, albeit at one-third the distance to the quasar. In a cursory examination of the objects to be analysed in our VLT/X-shooter survey, at least two additional BAL outflows show S IV/S IV* troughs.

Arav et al. (2013) also used the excited state from a high-ionization ion (O IV/O IV*) to determine the energetics of an outflow from quasar HE 0238−1904. Although the outflow did not show absorption from low-ionization ions, absorption from the very-high-ionization ions Ne VIII and Mg X confirmed the existence of a high-ionization phase. As discussed in the previous section, the S IV and P V absorption in SDSS J0831+0354 could originate from a separate ionization phase, but we cannot confirm its existence without absorption data from additional high-ionization ions.

### 5.4 Distance of quasar outflows from the central source

The outflow of SDSS J0831+0354 lies closer to the central source than the other outflows listed in Table 5. However, this distance ($R \sim 100$ pc) is three orders of magnitude greater than the trough forming region (0.01–0.1 pc) for accretion disc line-driven winds (e.g. fig. 3 of Murray et al. 1995; Proga, Stone & Kallman 2000). This large empirical distance scale is not limited to high $\dot{E}_k$ outflows. The large majority of measured distances to BAL (and narrower) outflows that were deduced using troughs from excited states yield distances between 10 and 10 000 pc (de Kool et al. 2001, 2002a,b; Hamann et al. 2001; Moe et al. 2009; Bautista et al. 2010; Dunn et al. 2010; Aoki et al. 2011; Edmonds et al. 2011; Borguet et al. 2012a,b; Arav et al. 2013; Lucy et al. 2014; Paper I). Two outflow components are found to be between 1 and 10 pc from the central source (de Kool et al. 2002a,b). The discrepancy between the empirical distances and those inferred from accretion disc line-driven winds models suggests that the latter models are not applicable to the trough formation of quasar outflows.

### 5.5 Reliability of measurements

Our group (Arav 1997; Arav et al. 1999a,b, 2001a,b; Arav, Korista & de Kool 2002; Arav et al. 2003; Scott et al. 2004; Gabel et al. 2005) and others (Barlow, Hamann & Sargent 1997; Hamann et al. 1997; Telfer et al. 1998; Churchill et al. 1999; Ganguly et al. 1999) showed that column densities derived from the AOD analysis of BAL troughs are unreliable when non-black saturation occurs in the troughs. For this reason, we use PC absorption models in this analysis.

**Table 6.** Sensitivity of derived energetics to input changes.

| Assumption | Effect(s) | Outcome | Reference |
|---|---|---|---|
| N(Si III)>$N_{AOD}$ | higher $N_H$, lower $U_H$ | higher $\dot{E}_k$ | Section 4.1 |
| $Z < 4\,Z_\odot$ | higher $N_H$ | higher $\dot{E}_k$ | Fig. 5 |
| Different SED | lower $N_H$ | lower $\dot{E}_k$ | Fig. 5 |
| $\Omega > 0.08$ | – | higher $\dot{E}_k$ | equation (5) |
| Two phases | higher $N_H$, higher $U_H$ | higher $\dot{E}_k$ | Section 5.2 |
| S IV* saturated | lower $n_H$, higher $R$ | higher $\dot{E}_k$ | Section 5.2 |

It is instructive to assess quantitatively the difference in $\dot{E}_k$ that arises from using these two absorption models on our results. To this end, we re-determine the photoionization solution using the AOD measurements for P V, Si III, Al III, and S IV (i.e. from the first column of Table 2). The resulting kinetic luminosity of $\dot{E}_k = 10^{45.6}$ erg s$^{-1}$ for the UV-Soft $4Z_\odot$ model differs only slightly from the $\dot{E}_k = 10^{45.7}$ erg s$^{-1}$ that we derive using the PC template. Thus, our results are rather insensitive to the method of column density extraction.

In Table 6, we demonstrate that almost all possible deviations from our representative model (UV-Soft SED, $Z = 4\,Z_\odot$, one ionization component, unsaturated Si III absorption) results in a higher $\dot{E}_k$ for the SDSS J0831+0354 outflow. Even with $\dot{E}_k$ lowered by assuming a different SED, the minimum energy allowed by our analysis is $\dot{E}_k/L_{Edd} = 2.6$ per cent for the HE0238 SED with $Z = 4\,Z_\odot$ (see Table 5).

## 6 SUMMARY

We present the analysis of BALQSO SDSS J0831+0354 using data obtained with VLT/X-shooter. Our main findings are as follows:

(1) The BAL outflow in SDSS J0831+0354 has a velocity of 10 800 km s$^{-1}$ in the rest frame of the quasar with a width of 3500 km s$^{-1}$ and shows kinematically connected absorption from the high-ionization species S IV and S IV*. The ratio of the excited column density to ground was used to determine the number density of the outflow to be $\log(n_e) = 4.42 \pm 0.24$ cm$^{-3}$.

(2) The non-black saturation of the P V doublet indicated that the absorber was inhomogenously distributed across the emission source. The saturation of the P V doublet resulted in a high ionic column density which, combined with the low elemental abundance of phosphorous, necessitates a high total hydrogen column density ($N_H$).

(3) Variations of the incident SED had only a small effect on the ionization solution ($U_H$,$N_H$) of the outflow, while an increased metallicity of $4Z_\odot$ lowered the required hydrogen column density by 0.4 dex. The UV-Soft SED with $Z = 4Z_\odot$ was adopted as the representative model, and the hydrogen column density was determined to be $\log(N_H) = 22.0 \pm 0.4$ cm$^{-2}$ with an ionization parameter of $\log(U_H) = -0.25 \pm 0.3$.

(4) The outflow was determined to be located 110 pc from the central source and contained a kinetic luminosity of 5.2 per cent of the Eddington luminosity of the quasar. We establish half of this value (2.6 per cent) as a conservative lower limit. This large kinetic luminosity makes the outflow of SDSS J0831+0354 a candidate

for quasar-mode AGN feedback effects seen in simulations (e.g. Hopkins et al. 2006; Ostriker et al. 2010).

## ACKNOWLEDGEMENT

We acknowledge support from NASA STScI grants GO 11686 and GO 12022 as well as NSF grant AST 1413319.

## REFERENCES

Aoki K., Oyabu S., Dunn J. P., Arav N., Edmonds D., Korista K. T., Matsuhara H., Toba Y., 2011, PASJ, 63, 457
Arav N., 1997, in Arav N., Shlosman I., Weymann R. J., eds, ASP Conf. Ser. Vol. 128, Mass Ejection from Active Galactic Nuclei. Astron. Soc. Pac., San Francisco, p. 208
Arav N., Korista K. T., de Kool M., Junkkarinen V. T., Begelman M. C., 1999a, ApJ, 516, 27
Arav N., Becker R. H., Laurent-Muehleisen S. A., Gregg M. D., White R. L., Brotherton M. S., de Kool M., 1999b, ApJ, 524, 566
Arav N., Brotherton M. S., Becker R. H., Gregg M. D., White R. L., Price T., Hack W., 2001a, ApJ, 546, 140
Arav N. et al., 2001b, ApJ, 561, 118
Arav N., Korista K. T., de Kool M., 2002, ApJ, 566, 699
Arav N., Kaastra J., Steenbrugge K., Brinkman B., Edelson R., Korista K. T., de Kool M., 2003, ApJ, 590, 174
Arav N. et al., 2007, ApJ, 658, 829
Arav N., Moe M., Costantini E., Korista K. T., Benn C., Ellison S., 2008, ApJ, 681, 954
Arav N., Borguet B., Chamberlain C., Edmonds D., Danforth C., 2013, MNRAS, 436, 3286
Ballero S. K., Matteucci F., Ciotti L., Calura F., Padovani P., 2008, A&A, 478, 335
Ballester P., Bramich D., Forchi V., Freudling W., Garcia-Dabó C. E., klein Gebbinck M., Modigliani A., Romaniello M., 2011, in Evans I. N., Accomazzi A., Mink D. J., Rots A. H., eds, ASP Conf. Ser. Vol. 442, Astronomical Data Analysis Software and Systems XX. Astron. Soc. Pac., San Francisco, p. 261
Barlow T. A., Hamann F., Sargent W. L. W., 1997, in Arav N., Shlosman I., Weymann R. J., eds, ASP Conf. Ser. Vol. 442, Mass Ejection from Active Galactic Nuclei. Astron. Soc. Pac., San Francisco, p. 13
Bautista M. A., Dunn J. P., Arav N., Korista K. T., Moe M., Benn C., 2010, ApJ, 713, 25
Borguet B. C. J., Edmonds D., Arav N., Dunn J., Kriss G. A., 2012a, ApJ, 751, 107
Borguet B. C. J., Edmonds D., Arav N., Benn C., Chamberlain C., 2012b, ApJ, 758, 69
Borguet B. C. J., Arav N., Edmonds D., Chamberlain C., Benn C., 2013, ApJ, 762, 49 (Paper I)
Cardelli J. A., Clayton G. C., Mathis J. S., 1989, ApJ, 345, 245
Cattaneo A. et al., 2009, Nature, 460, 213
Choi E., Naab T., Ostriker J. P., Johansson P. H., Moster B. P., 2014, MNRAS, 442, 440
Churchill C. W., Mellon R. R., Charlton J. C., Jannuzi B. T., Kirhakos S., Steidel C. C., Schneider D. P., 1999, ApJ, 519, L43
Ciotti L., Ostriker J. P., Proga D., 2009, ApJ, 699, 89
Ciotti L., Ostriker J. P., Proga D., 2010, ApJ, 717, 708
Dai X., Shankar F., Sivakoff G. R., 2008, ApJ, 672, 108
Dai X., Shankar F., Sivakoff G. R., 2012, ApJ, 757, 180
de Kool M., Arav N., Becker R. H., Gregg M. D., White R. L., Laurent-Muehleisen S. A., Price T., Korista K. T., 2001, ApJ, 548, 609
de Kool M., Becker R. H., Gregg M. D., White R. L., Arav N., 2002a, ApJ, 567, 58
de Kool M., Becker R. H., Arav N., Gregg M. D., White R. L., 2002b, ApJ, 570, 514
Di Matteo T., Springel V., Hernquist L., 2005, Nature, 433, 604
Dunn J. P. et al., 2010, ApJ, 709, 611
Dunn J. P., Arav N., Aoki K., Wilkins A., Laughlin C., Edmonds D., Bautista M., 2012, ApJ, 750, 143
Edmonds D. et al., 2011, ApJ, 739, 7
Elvis M., 2006, Mem. Soc. Astron. Italiana, 77, 573
Ferland G. J. et al., 2013, Rev. Mexic. de Astron. y Astrof., 49, 137
Gabel J. R. et al., 2005, ApJ, 623, 85
Gabel J. R., Arav N., Kim T., 2006, ApJ, 646, 742
Ganguly R., Eracleous M., Charlton J. C., Churchill C. W., 1999, AJ, 117, 2594
Ganguly R., Brotherton M. S., 2008, ApJ, 672, 102
Germain J., Barai P., Martel H., 2009, ApJ, 704, 1002
Gilkis A., Soker N., 2012, MNRAS, 427, 1482
Hamann F., Ferland G., 1993, ApJ, 418, 11
Hamann F., Barlow T. A., Junkkarinen V., Burbidge E. M., 1997, ApJ, 478, 80
Hamann F. W., Barlow T. A., Chaffee F. C., Foltz C. B., Weymann R. J., 2001, ApJ, 550, 142
Hewett P. C., Foltz C. B., 2003, AJ, 125, 1784
Hopkins P. F., Elvis M., 2010, MNRAS, 401, 7
Hopkins P. F., Hernquist L., Cox T. J., Di Matteo T., Robertson B., Springel V., 2006, ApJS, 163, 1
Hopkins P. F., Murray N., Thompson T. A., 2009, MNRAS, 398, 303
Knigge C., Scaringi S., Goad M. R., Cottis C. E., 2008, MNRAS, 386, 1426
Krolik J. H., 1999, Active Galactic Nuclei : from the Central Black Hole to the Galactic Environment, Princeton Univ. Press, Princeton, NJ
Landi E., Young P. R., Dere K. P., Del Zanna G., Mason H. E., 2013, ApJ, 763, 86
Levine R., Gnedin N. Y., 2005, ApJ, 632, 727
Lucy A. B., Leighly K. M., Terndrup D. M., Dietrich M., Gallagher S. C., 2014, ApJ, 783, 58
Luo B. et al., 2014, ApJ, 794, 70
Moe M., Arav N., Bautista M. A., Korista K. T., 2009, ApJ, 706, 525
Murray N., Chiang J., Grossman S. A., Voit G. M., 1995, ApJ, 451, 498
Ostriker J. P., Choi E., Ciotti L., Novak G. S., Proga D., 2010, ApJ, 722, 642
Park D., Woo J.-H., Denney K. D., Shin J., 2013, ApJ, 770, 87
Proga D., Stone J. M., Kallman T. R., 2000, ApJ, 543, 686
Scannapieco E., Oh S. P., 2004, ApJ, 608, 62
Schlegel D. J., Finkbeiner D. P., Davis M., 1998, ApJ, 500, 525
Scott J. E. et al., 2004, ApJS, 152, 1
Silk J., Rees M. J., 1998, A&A, 331, L1
Telfer R. C., Kriss G. A., Zheng W., Davidsen A. F., Green R. F., 1998, ApJ, 509, 132
Vestergaard M., Osmer P. S., 2009, ApJ, 699, 800
Weymann R. J., Carswell R. F., Smith M. G., 1981, ARA&A, 19, 41
Weymann R. J., Morris S. L., Foltz C. B., Hewett P. C., 1991, ApJ, 373, 23
Zubovas K., Nayakshin S., 2014, MNRAS, 440, 2625

This paper has been typeset from a TEX/LATEX file prepared by the author.